IEEE Access
Multidisciplinary | Rapid Review | Open Access Journal

SPECIAL SECTION ON GREEN COMMUNICATIONS AND NETWORKING FOR 5G WIRELESS

Received September 13, 2016, accepted October 3, 2016, date of publication October 5, 2016, date of current version November 8, 2016.

Digital Object Identifier 10.1109/ACCESS.2016.2615425

Vehicle Positioning Using 5G Millimeter-Wave Systems

XUERONG CUI[1], (Member, IEEE), THOMAS AARON GULLIVER[2], (Senior Member, IEEE), JUAN LI[1], AND HAO ZHANG[2,3]

[1]Department of Computer and Communication Engineering, China University of Petroleum (East China), Qingdao 266580, China
[2]Department of Electrical and Computer Engineering, University of Victoria, Victoria, BC V8W 2Y2, Canada
[3]Department of Electrical Engineering, Ocean University of China, Qingdao 266100, China

Corresponding author: X. Cui (cuixuerong@163.com)

This work was supported in part by the Nature Science Foundation of China under Grant 61301139 and Grant 61671482, in part by the Nature Science Foundation of Shandong Province under Grant ZR2014FL014 and Grant ZR2014FM017, in part by the Fundamental Research Funds for the Central Universities under Grant 16CX02046A, and in part by the Project of Basic Research Application of Qingdao City under Grant 14-2-4-83-jch.

ABSTRACT Recent growth in traffic and the resulting congestion and accidents has increased the demand for vehicle positioning systems. Existing global navigation satellite systems were designed for line of sight environments and thus accurately determining the location of a vehicle in urban areas with tall buildings or regions with dense foliage is difficult. Fifth generation (5G) cellular networks provide device-to-device communication capabilities which can be exploited to determine the real-time location of vehicles. Millimeter-wave (mmWave) transmission is regarded as a key technology for 5G networks. This paper examines vehicle positioning using 5G mmWave signals. Both a correlation receiver and an energy detector are considered for timing estimation. Furthermore, fixed and dynamic thresholds for energy detection are examined. It is shown that a correlation receiver can provide excellent ranging accuracy but has high computational complexity, whereas an energy detector has low computational complexity and provides good ranging accuracy. Furthermore, the Gaussian raised-cosine pulse (RCP), Gaussian pulse, and Sinc-RCP impulse radio waveforms provide the best performance.

INDEX TERMS Position measurement, vehicular and wireless technologies, millimeter wave communication, intelligent transportation systems, 5G.

I. INTRODUCTION

A recent report [1] by the World Health Organization indicates that the number of road traffic deaths worldwide has reached an unacceptably high level of over one million per year. Further, this has become the leading cause of death for young people aged 15–29. Current trends suggest that by 2030 traffic accidents will become the fifth greatest cause of death unless urgent action is taken. For vehicular Ad-Hoc network [2], the most promising means of mitigation is the development of cooperative collision avoidance (CCA) and emergency warning message (EWM) systems that allow vehicles to detect potential hazards and take steps to avoid accidents by sharing information such as location, speed, and acceleration. These systems require low latency and high reliability or their routing algorithm [3], particularly with respect to the location of neighboring vehicles. However, accurately determining vehicle locations is still a significant challenge [4]. Without this information, it will not be possible to provide timely warning of potential dangers, and false warnings will be generated, causing a lack of confidence in the systems.

Currently, global navigation satellite systems such as the global positioning system (GPS), global navigation satellite system (GLONASS) [5] and BeiDou satellite positioning system (BDS) [6] are widely used in vehicles but are accurate only in open areas which are free of obstructions. This is because these systems were designed for line of sight (LOS) environments. They are inaccurate in non-line of sight (NLOS) environments such as tunnels or urban areas with tall buildings. Thus, these systems must be integrated with other techniques such as short range wireless positioning [7]–[9] in wireless sensor networks [10], [11] to improve the accuracy. For example, a Chinese area positioning system (CAPS) based on ultra wideband (UWB) signals has been proposed [12].

Fifth generation (5G) cellular networks are being developed to support a variety of innovative applications [13] such as device-to-device (D2D) communications. In order to meet

the explosive increase in demand for bandwidth in these networks, millimeter-wave (mmWave) transmission has been proposed. Measurement results show that the frequency range 28-38 GHz can be employed with directional antennas in the base stations and mobile devices [14]. Samsung Electronics [15] has achieved a data rate of 1.2 Gbps at 28 GHz with a vehicle traveling at over 100 km/h. Measurements at 28 GHz and 73 GHz in the dense New York urban environment have been used to derive detailed statistical channel models [16]. It was found that even in NLOS environments, sufficient signal levels can be obtained at distances up to 200 m. Further, mmWave signals can provide centimeter level ranging accuracy [17]. The mmWave bands are also being considered for local multipoint distribution services (LMDS). At 28 GHz, 38 GHz, and 60 GHz, there is 1 GHz, 2 GHz and 7 GHz of bandwidth available, respectively [18]. One advantage of 28 GHz is that the signals have better penetration, so this frequency is considered in this paper.

A number of waveforms have been considered for 5G systems. The European research project 5GNOW has proposed a multicarrier waveform to support the diverse requirements of 5G applications. In [19], the time-frequency efficiency of three candidate 5G multicarrier waveforms, namely filtered cyclic prefix orthogonal frequency division multiplexing (CP-OFDM), filter bank multicarrier (FBMC), and universal filtered multicarrier (UFMC), were examined. However, impulse radio (IR) waveforms were not considered. IR waveforms can provide very accurate positioning, even in dense multipath, NLOS fading environments, and thus are better suited for this application than multicarrier waveforms. This is because of the fine multipath and precise time resolution (sub-nanosecond to nanosecond), due to the transmission of very short pulses. In addition, the wide signal bandwidth results in a very low power spectral density, which reduces interference to other radio frequency (RF) systems. The short pulse duration reduces or eliminates the distortion and spurious signal detections due to multipath propagation. These signals can also penetrate many obstacles to provide a LOS signal. The IEEE 802.15.4a UWB standard [20] specifies a wireless physical layer using IR-UWB signaling to enable precision ranging. However, the ranging performance of mmWave waveforms has not been examined. Therefore, this paper considers six mmWave waveforms for positioning applications, namely the Gaussian pulse, inverse fast Fourier transform (IFFT) pulse, Gaussian raised-cosine pulse (Gaussian-RCP), Hann-RCP, Sinc-RCP, and rectangular-RCP. These waveforms are employed in a pulse position modulation (PPM) system. Both a correlation receiver and an energy detector [21], [22] with fixed and dynamic thresholds are considered for ranging. The skewness of the energy values is employed to improve the ranging accuracy with a dynamic threshold.

The focus of this paper is on IR mmWave waveforms for vehicle positioning. The main contributions include:

1) MmWave signals and the corresponding power spectral densities (PSDs) are examined for future 5G cellular networks.
2) The ranging accuracy of mmWave signals is evaluated and compared using a correlation receiver and an energy detector based on threshold crossing. The Gaussian-RCP, Gaussian pulse, and Sinc-RCP waveforms are shown to provide the best ranging performance. The computational complexity of a correlation receiver makes it less desirable for real-time vehicle positioning.

The remainder of this paper is organized as follows. In Section 2, six mmWave waveforms are examined. Section 3 presents the system model and the simulation parameters. Section 4 introduces the ranging methods that will be considered, namely a correlation receiver and an energy detector with fixed and dynamic thresholds. Performance results are given in Section 5 to evaluate and compare the waveforms and ranging methods. Finally, Section 6 concludes the paper.

II. MILLIMETER-WAVE (mmWave) WAVEFORMS

Both carrier and carrierless waveforms are employed in impulse radio (IR) systems. Carrierless waveforms include Gaussian and IFFT pulses, while carrier waveforms typically have a raised-cosine pulse (RCP) shape such as Gaussian-RCP, Hann-RCP, Sinc-RCP and Rectangular-RCP. The RCP waveforms are given by

$$p(t) = h(t)\cos(2\pi f_c t) \tag{1}$$

where $h(t)$ is the baseband pulse, and f_c is the carrier or center frequency.

A. GAUSSIAN PULSE WAVEFORM

The Gaussian pulse and its derivatives are frequently used as mmWave waveforms and can be expressed as

$$\begin{aligned} g_0(t) &= Ae^{-\frac{2\pi t^2}{\alpha^2}}, \\ g_1(t) &= A(-\frac{4\pi t}{\alpha^2})e^{-\frac{2\pi t^2}{\alpha^2}}, \\ g_2(t) &= A\frac{4\pi t}{\alpha^4}e^{-\frac{2\pi t^2}{\alpha^2}}(-\alpha^2 + 4\pi t^2), \\ &\vdots \qquad\qquad \vdots \end{aligned} \tag{2}$$

where $g_0(t)$ is the Gaussian pulse, $g_k(t)$ is the kth derivative of $g_0(t)$, $k \geq 1$, and A is a constant used to normalize the pulse energy. α is the shaping factor which affects both the bandwidth and f_c. The relationship between α, k and f_c is

$$f_c = \frac{\sqrt{k}}{\alpha\sqrt{\pi}} \tag{3}$$

Thus, changing α or k will change the PSD of the waveform as well as f_c. Figures 1 and 2 show Gaussian pulses with pulse duration $T_p = 0.5$ ns, $k = 15$, and $\alpha = 1.1 \times 10^{-10}$ for $f_c = 28$ GHz, $\alpha = 8.1 \times 10^{-11}$ for $f_c = 38$ GHz,

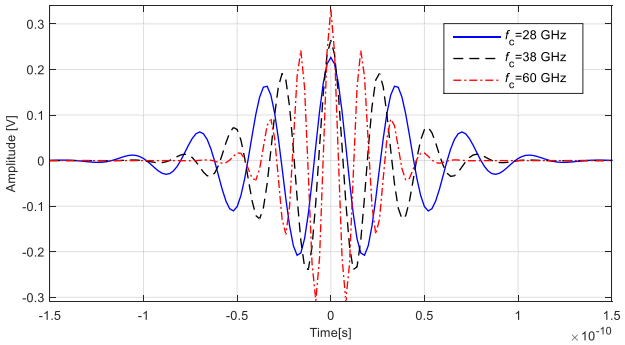

FIGURE 1. The 15th derivative Gaussian pulse waveform for three values of f_c.

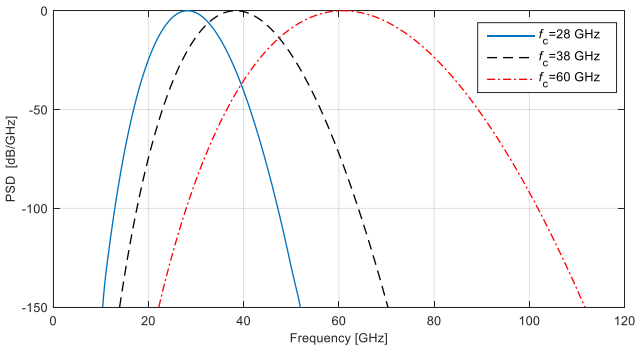

FIGURE 2. PSD of the 15th derivative Gaussian pulse waveform for three values of f_c.

and $\alpha = 5.1 \times 10^{-11}$ for $f_c = 60$ GHz. These results show that a smaller value of α results in a shorter pulse duration, higher center frequency, and larger bandwidth.

B. IFFT PULSE WAVEFORM

A pulse waveform can be obtained by taking the inverse fast Fourier transform (IFFT) of the desired spectral mask. For example, assuming a maximum power of 10 W, the PSD is given by

$$P(f) \approx \begin{cases} \sqrt{\frac{10T_p}{f_H - f_L}} & f_L \le f \le f_H \\ 0 & \text{otherwise,} \end{cases} \tag{4}$$

where f_L and f_H are the desired low and high frequencies, respectively. Taking the IFFT of (3) gives the pulse waveform

$$h(t) = \frac{\sqrt{10T_p}}{2\pi\sqrt{f_H - f_L}} \left(f_H sinc(2f_H t) - f_L sinc(2f_L t)\right), \quad t \in [-\frac{T_p}{2}, \frac{T_p}{2}], \tag{5}$$

where $\text{sinc}(x) = \sin(\pi x)/\pi x$.

Figure 3 shows the IFFT pulse for $f_L = 27.5$ GHz, $f_H = 31.5$ GHz, and $T_p = 0.5$ ns and 5 ns. T_p determines the number of sidelobes in the pulse. When $T_p = 0.5$ ns, there are no sidelobes, and as T_p increases the number of sidelobes increases. Figure 4 shows the PSD of the 28 GHz pulse as well as a 60 GHz pulse with $f_L = 57$ GHz and

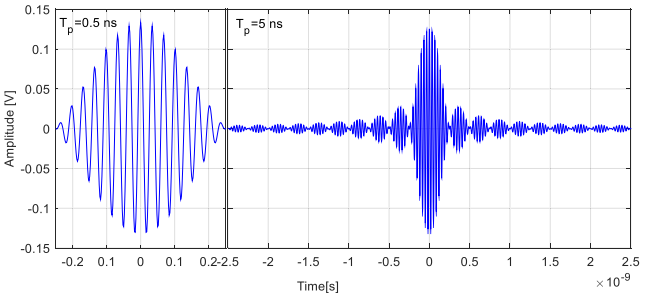

FIGURE 3. The IFFT pulse waveform for two values of T_p with $f_c = 28$ GHz.

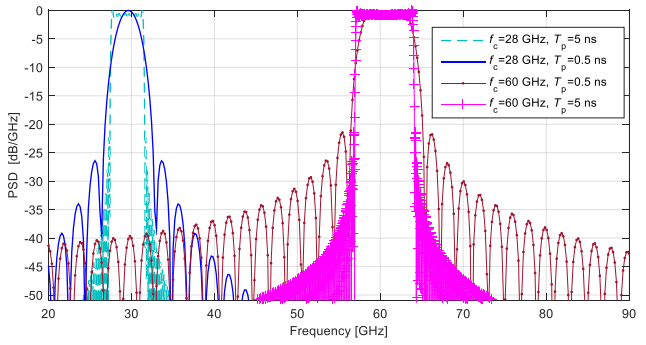

FIGURE 4. PSD of the IFFT pulse waveform for different values of f_c and T_p.

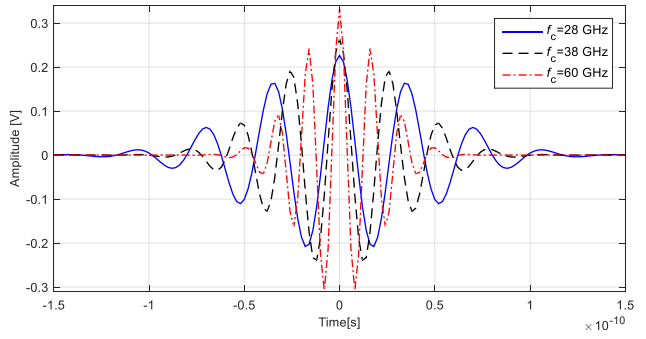

FIGURE 5. The Gaussian-RCP pulse waveform for three values of f_c.

$f_H = 64$ GHz. When $T_p = 5$ ns, there are more sidelobes than with $T_p = 0.5$ ns.

C. GAUSSIAN-RCP WAVEFORM

The raised-cosine pulse (RCP) waveform given in (1) is considered using the Gaussian pulses in (2), with $h(t) = g_0(t)$ and $A = 1$. The parameters α and k can be used to adjust the bandwidth and f_c. Figures 5 and 6 show the Gaussian-RCP pulse waveform and corresponding PSD with $t \in [-T_p/2, T_p/2]$, $T_p = 0.5$ ns, and $\alpha = 0.11 \times 10^{-9}$ for $f_c = 28$ GHz, 38 GHz, and 60 GHz.

D. HANN-RCP WAVEFORM

The baseband signal of the Hann-RCP waveform is given by

$$h(t) = 0.5(1 - \cos(2\pi f_s t)), \quad t \in [0, T_p], \tag{6}$$

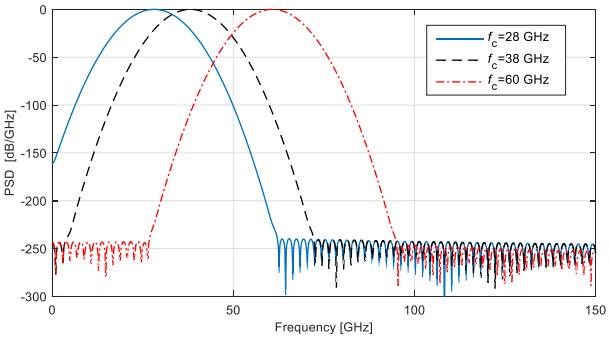

FIGURE 6. PSD of the Gaussian-RCP pulse waveform for three values of f_c.

where $f_s = 1/T_p$. The corresponding PSD is

$$P(f) = \frac{T_p \text{sinc}^2(fT_p)}{4\left(1 - f^2 T_p^2\right)^2}. \tag{7}$$

Figure 7 shows the Hann-RCP pulse waveform and corresponding PSD with $f_c = 28$ GHz, and $T_p = 0.5$ ns and 5 ns. The bandwidth with $T_p = 0.5$ ns is smaller than with $T_p = 5$ ns.

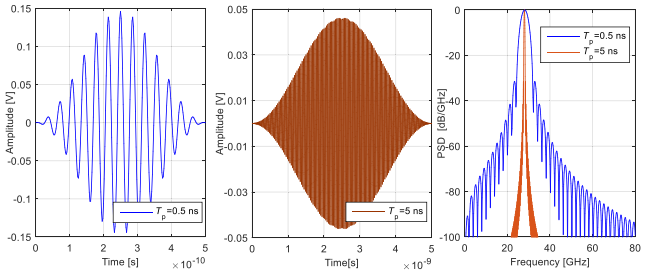

FIGURE 7. The Hann-RCP pulse waveform and PSD for two values of T_p.

E. SINC-RCP WAVEFORM

The baseband signal of the sinc-RCP pulse is given by

$$h(t) = sin\left(\frac{\pi t}{T}\right) / \frac{\pi t}{T} \quad t \in [-\frac{T_p}{2}, \frac{T_p}{2}]. \tag{8}$$

where T determines the number of sidelobes in a pulse duration. When $T = T_p/4$ there is one sidelobe on each side of the mainlobe, and as T decreases the number of sidelobes increases. The corresponding PSD is

$$P(f) = \frac{T_p}{16\pi^2}\left|S_i\left(2\pi + \pi f T_p\right) - S_i\left(-2\pi + \pi f T_p\right)\right|^2, \tag{9}$$

where $S_i(x) = \int_0^x \sin t / t \, dt$. Figure 8 presents the sinc-RCP pulse waveform and corresponding PSD for $f_c = 28$ GHz with $T = T_p/4$ and $T_p/8$. This shows that as T decreases, the bandwidth increases.

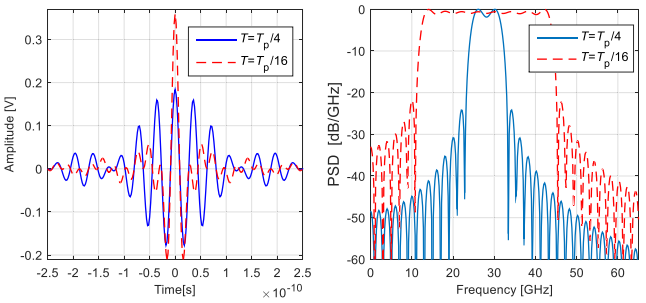

FIGURE 8. The Sinc-RCP pulse waveform and PSD for two values of T.

F. RECTANGULAR-RCP WAVEFORM

The baseband signal of the rectangular-RCP pulse is defined as

$$h(t) = \begin{cases} 1 & t \in [-\frac{T_p}{2}, \frac{T_p}{2}] \\ 0 & \text{otherwise}, \end{cases} \tag{10}$$

with PSD

$$P(f) = T_p sinc^2\left(fT_p\right). \tag{11}$$

Figure 9 presents the waveform and corresponding PSD of the Rectangular-RCP pulse with $f_c = 28$ GHz, and $T = 0.5$ ns.

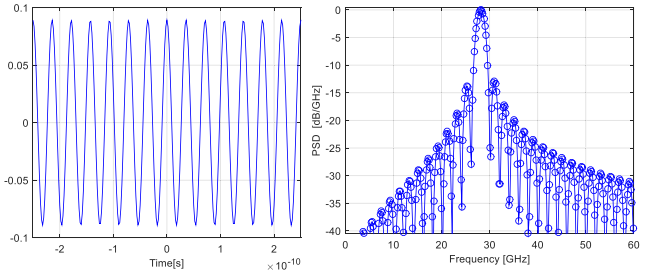

FIGURE 9. The Rectangular-RCP waveform and corresponding PSD.

III. SYSTEM MODEL

The system model is presented in this section. This model includes the pulse shaping, modulation, channel, and receiver. The parameters for the six pulse shapes considered are given in Table 1.

With pulse position modulation (PPM), the transmitted signal can be expressed as

$$s(t) = \sum_{-\infty}^{+\infty} p\left(t - jT_f - a_j\varepsilon\right), \tag{12}$$

where j and T_f are the index and frame duration, respectively, and ε is the PPM time shift so that if $a_j = 1$, the signal will be shifted, and otherwise there is no time shift. The PPM parameters employed in this paper are given in Table 2.

Considering multiple vehicles to be positioned, pulse position modulation with time hopping (PPM-TH) can be

TABLE 1. Pulse waveform parameters.

Parameter	Value
Center frequency, f_c	28 GHz
Low frequency, f_L	27.5 GHz
High frequency, f_H	31.5 GHz
Pulse duration, T_p	0.5 ns
Sampling frequency, f_s	500 GHz
Gaussian-RCP shaping factor, α	0.125 ns
Gaussian pulse shaping factor, α	0.11 ns
Gaussian pulse derivative, k	15
T for Sinc-RCP	1 ns

TABLE 2. PPM parameters.

Parameter	Value
Chip time, T_c	5 ns
PPM time shift, ε	0.2 ns
Frame duration, T_f	5 ns

employed, in which case the transmitted signal can be expressed as

$$s(t) = \sum_{-\infty}^{+\infty} p\left(t - jT_f - c_j T_c - a_j \varepsilon\right), \tag{13}$$

where T_c is the chip duration. Time hopping is achieved via a pseudorandom integer-valued sequence c_j, which differs for each user to allow for multiple access communications.

In a multipath channel, the signal may be scattered, reflected, and diffracted, which causes fading. To date, there is no generally accepted 5G channel model. However, the AWGN channel can be considered as a baseline for communication systems. In this case, the received signal can be written as

$$r(t) = Gs(t-\tau) + n(t) \tag{14}$$

where $s(t)$ is the transmitted signal, G is the channel gain, τ is the delay, and $n(t)$ is AWGN with PSD N_0. Because of the motion of vehicles, a Doppler frequency shift exists which is given by

$$f_d = v * f_c / C, \tag{15}$$

where v is the relative speed of the vehicle and C is the speed of electromagnetic wave.

IV. POSITION ESTIMATION METHODS

In general, there are two kinds of positioning techniques, range based and non-range based. Time of arrival (TOA) [23] and time difference of arrival (TDOA) [24] are range based methods, while fingerprinting based on the received signal strength (RSS) [25], [26] and angle of arrival (AOA) [27] are non-range based methods. Range based TOA positioning techniques are more suitable for IR communication systems as they can exploit the high time resolution possible with the short mmWave signals [28].

In TOA positioning, the time for a signal to travel between nodes can be used to estimate the distance between them. This can be obtained in cellular networks using base station locations [29] and in infrastructureless or ad hoc networks using anchor or reference node locations [30], [31]. TOA positioning is also called circle localization in two dimensions (2D) or spherical localization in three dimensions (3D). For example, in 2D the range between a target node and a base station can be seen as the radius of a circle centered at the base station as shown in Fig. 10. In this figure, the base stations are located at (X_1, Y_1), (X_2, Y_2) and (X_3, Y_3), and the corresponding radii are D_1, D_2 and D_3. The estimated position is the joint intersection of the circles. Positioning in 2D space requires at least 3 base stations, and in 3D space at least 4 base stations.

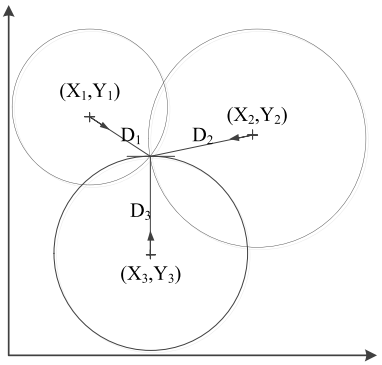

FIGURE 10. TOA positioning in two dimensions (2D).

In 3D, the coordinates (x, y, z) of a target node can be determined by solving the system of equations

$$\begin{Bmatrix} \sqrt{(X_1-x)^2+(Y_1-y)^2+(Z_1-z)^2} \\ \sqrt{(X_2-x)^2+(Y_2-y)^2+(Z_2-z)^2} \\ \cdots\cdots \\ \sqrt{(X_k-x)^2+(Y_k-y)^2+(Z_k-z)^2} \end{Bmatrix} = \begin{Bmatrix} D_1 \\ D_2 \\ \cdots\cdots \\ D_k \end{Bmatrix}, \tag{16}$$

where (X_k, Y_k, Z_k) is the position of the kth base station, and D_k is the range from the target node. Errors exist in the D_k due to clock drift, noise, fading, and Doppler shifts. The effects of these errors can be mitigated using methods such as least-squares estimation (LSE), the Chan algorithm, the Taylor algorithm, or Kalman filtering [32]. For convenience,

(16) can be expressed as

$$AI = b, \tag{17}$$

where

$$A = -2\begin{bmatrix} (X_1 - X_k) & (Y_1 - Y_k) & (Z_1 - Z_k) \\ (X_2 - X_k) & (Y_2 - Y_k) & (Z_2 - Z_k) \\ & \cdots\cdots & \\ (X_{k-1} - X_k) & (Y_{k-11} - Y_k) & (Z_{k-11} - Z_k) \end{bmatrix}, \tag{18}$$

$$I = -2\begin{bmatrix} x \\ y \\ z \end{bmatrix}, \tag{19}$$

and

$$b = \begin{bmatrix} D_1^2 - D_k^2 - X_1^2 + X_k^2 - Y_1^2 + Y_k^2 - Z_1^2 + Z_k^2 \\ D_2^2 - D_k^2 - X_2^2 + X_k^2 - Y_2^2 + Y_k^2 - Z_2^2 + Z_k^2 \\ \cdots\cdots \\ D_{k-1}^2 - D_k^2 - X_{k-1}^2 + X_k^2 - Y_{k-1}^2 + Y_k^2 - Z_{k-1}^2 + Z_k^2 \end{bmatrix}. \tag{20}$$

Then the coordinates of the target node can be obtained from

$$I = A^{-1}b. \tag{21}$$

Accurate range estimation is the key to precise positioning, so the focus here is on ranging with different IR waveforms. The two main types of ranging algorithms, namely correlation receiver and energy detector, are now presented.

A. CORRELATION RECEIVER

The goal of range estimation is to obtain an unbiased estimate of the TOA $\hat{\tau}$ from the received signal $r(t)$. If the received signal $r(t)$ is sampled at a frequency f_s, the resulting signal can be expressed as

$$R[i] = r(i/f_s), \quad i = 0, 1, 2, \ldots \tag{22}$$

A correlator receiver is used to correlate a referenced template S with R, then the unbiased estimate of $\hat{\tau}$ corresponds to the position $\hat{m}$ of the correlation peak which is given by

$$\hat{m} = argmax\{\sum_i R[i] \times S[i-m]\} \tag{23}$$

The range estimate is then

$$\hat{d} = C \times \hat{m}/f_s \tag{24}$$

A correlation receiver is optimal for TOA estimation, but sampling at the Nyquist rate has high computational complexity. In addition, *a priori* channel estimation is required, including the amplitude, delay, and phase of each multipath component. Because of the channel estimation and sampling rate requirements, a correlation receiver may not be practical for vehicular positioning applications. In [33], the IEEE 802.11p standard was employed with OFDM modulation for vehicle positioning. This required computing the cross-correlation between the received signal and the short preamble. Thus, this technique is specific to the standard and the performance is dependent on the preamble length, which is fixed.

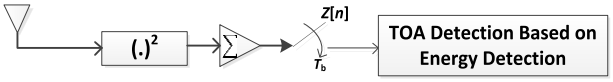

FIGURE 11. Block diagram of the energy detection receiver.

B. ENERGY DETECTION WITH A FIXED THRESHOLD

As opposed to the complex correlation receiver, energy detection is a simple non-coherent method for TOA estimation. An energy detector consists of a square-law device, an integrator with integration period T_b, and a decision mechanism, as shown in Fig. 11. The integrator output or energy value $Z[n]$ can be expressed as

$$Z[n] = \sum_{i=(n-1)T_b f_s}^{nT_b f_s - 1} |R(i)|^2, \tag{25}$$

where $n = 1, 2, \ldots, N_b$ is the sample index with respect to each integration period. Because of inter-frame leakage due to the multipath channel, the integration duration is set to $2T_f$ so that $N_b = (2T_f)/T_b$. The TOA estimate is obtained by comparing the integrator output with a threshold. This solution has low complexity because a low sampling rate can be employed and channel estimation is not required.

One of the simplest energy detection estimation methods is maximum energy selection (MES), where the maximum energy value is considered as the start of the signal or the time of arrival. Then the TOA estimate as

$$\tau_{MES} = [\min\{n | Z[n] = \max(Z)\} - 0.5] \times T_b \tag{26}$$

However, the maximum value may not correspond to the first arriving signal component, particularly in NLOS environments. As shown in Fig. 12, the first energy value (corresponding to the actual TOA), may be located before the maximum value $Z[n_{\max}]$, i.e. $\hat{n} \leq n_{\max}$. In this case, an appropriate threshold should be selected to estimate the TOA, and the technique is called threshold crossing (TC) TOA estimation. The received energy values are compared with the

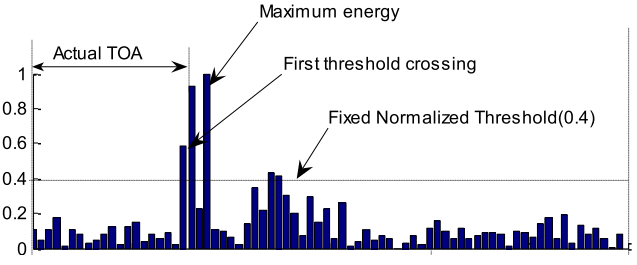

FIGURE 12. TOA estimation based on the received energy.

threshold $\xi \in (0, 1]$, and the first energy value crossing this threshold is considered as the TOA estimate, given by

$$\tau_{TC} = [\min\{n|Z[n] \geq \xi \times \max(Z)\} - 0.5] \times T_b \quad (27)$$

A fixed threshold is often employed, for example $\xi = 0.6$, and if $\xi = 1$ this method is the same as MES.

C. ENERGY DETECTION WITH A DYNAMIC THRESHOLD

It is difficult to determine an appropriate fixed threshold ξ for all channel environments, in which case a dynamic threshold can be employed. The problem is then how to obtain a suitable threshold, i.e. how to establish a relationship between the energy detector values and ξ. In [34], a dynamic threshold was proposed based on the statistics of UWB signals. In this paper, the threshold is obtained based on the standard deviation and skewness of the mmWave signal energy values.

1) STATISTICS OF THE ENERGY DETECTOR VALUES

The standard deviation and skewness are measures of signal variability and are given by

$$\sigma = \sqrt{\frac{1}{N_b - 1} \sum_{i=1}^{N_b} (Z_i - \bar{Z})^2}, \quad (28)$$

and

$$S = \frac{1}{(N_b - 1)\,\sigma^3} \sum_{i=1}^{N_b} (Z_i - \bar{Z})^3, \quad (29)$$

respectively, where $\overline{Z}$ is the mean of the energy values If these values have a normal distribution, the skewness will be 0, in fact this occurs for any symmetric distribution.

2) STATISTICAL CHARACTERISTICS OF THE ENERGY VALUES

In order to examine the statistical characteristics of the energy values, for each SNR value, 1000 channel realizations were generated with an integration period $T_b = T_f/30$=0.1667 ns. Figure 13 shows that the standard deviation is not monotonic for the six waveforms, but the skewness shown in Fig. 14 is monotonic. Further, the change in the skewness is significant for SNR values between 10 dB and 25 dB. This

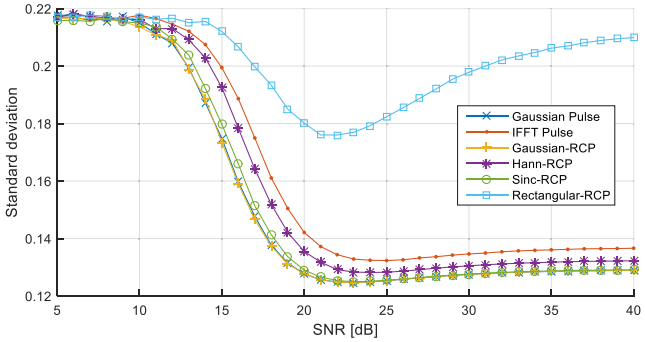

FIGURE 13. Standard deviation of the energy values.

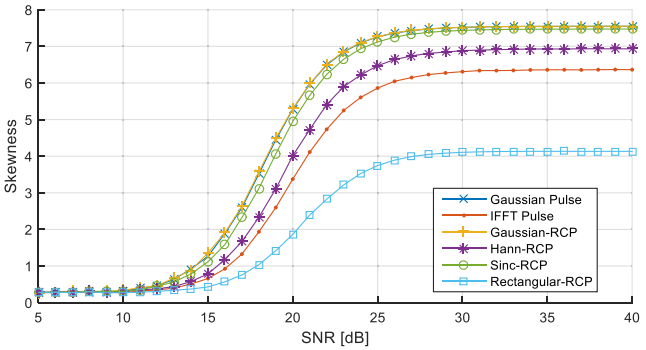

FIGURE 14. Skewness of the energy values.

variation is greater than that of the standard deviation from 10 dB to 20 dB. Therefore, skewness is a better choice to determine the threshold.

3) CURVE FITTING FOR THE THRESHOLD

In order to fit the curve of skewness versus threshold, 2000 realizations for each SNR=4, 5, ..., 40 dB were generated with thresholds $\xi = 0.1, 0.2, \ldots, 1$. For each realization, the threshold with least estimation error was selected as the best threshold ξ_{best}. Then the best threshold was determined for each skewness value. A degree three polynomial was fit using the least-squares method to provide a threshold ξ for each skewness value S, where S is the x-coordinate and ξ is the y-coordinate. The coefficients of the polynomial were generated by minimizing the sum of the squares of the residuals. The$i$th residual r_i for the ith pair (S, ξ) is defined as

$$r_i = y_i - \hat{y}_i \quad (30)$$

where y_i is the best threshold and $\hat{y}_i$ is the fitted threshold for the ith pair. The sum of the squares of the residuals is given by

$$S_s = \sum_{i=1}^{n} r_i^2 = \sum_{i=1}^{n} (y_i - \hat{y}_i)^2 \quad (31)$$

where n is the number of pairs (S, ξ_{best}). The corresponding polynomials for the 6 waveforms are

$$\begin{aligned}
\xi &= -0.0014S^3 + 0.0207S^2 - 0.1650S + 0.7777 \\
&\quad \text{(Gaussian Pulse)}, \\
\xi &= -0.0034S^3 + 0.0421S^2 - 0.2140S + 0.8007 \\
&\quad \text{(IFFT Pulse)}, \\
\xi &= -0.0006S^3 + 0.0147S^2 - 0.1593S + 0.7787 \\
&\quad \text{(Gaussian-RCP)}, \\
\xi &= -0.0013S^3 + 0.0221S^2 - 0.1765S + 0.7903 \\
&\quad \text{(Hann-RCP)}, \\
\xi &= -0.0019S^3 + 0.0263S^2 - 0.1839S + 0.7934 \\
&\quad \text{(Sinc-RCP)}, \\
\xi &= 0.0009S^3 - -0.0002S^2 - 0.1590S + 0.8090 \\
&\quad \text{(Rectangular-RCP)}. \quad (32)
\end{aligned}$$

V. PERFORMANCE RESULTS AND DISCUSSION

In this section, the ranging performance with the mmWave waveforms is evaluated using the mean absolute error (MAE) which is given by

$$MAE = C \times \frac{1}{N} \sum_{n=1}^{N} \left| t_n - \hat{t}_n \right|, \tag{33}$$

where t_n is the nth actual propagation time, $\hat{t}_n$ is the nth TOA estimate, C is the speed of electromagnetic wave, and N is the number of ranging estimates. With a vehicle speed of $v = 240$ km/hour, from (15), the Doppler shift is $f_d = 6.22$ kHz.

A. CORRELATION RECEIVER PERFORMANCE

The MAE performance of the six waveforms was determined using the correlation receiver with 2000 realizations for each value of SNR=0, 1, ..., 20 dB, and the results are presented in Fig. 15. This shows that the performance of the Gaussian-RCP, Gaussian Pulse, and Sinc-RCP waveforms is similar, whereas the Rectangular-RCP and IFFT waveforms have the worst performance. When SNR=0 dB, the MAE with the Rectangular-RCP waveform is nearly 0.01 m, which is more than twice that of the Gaussian-RCP waveform.

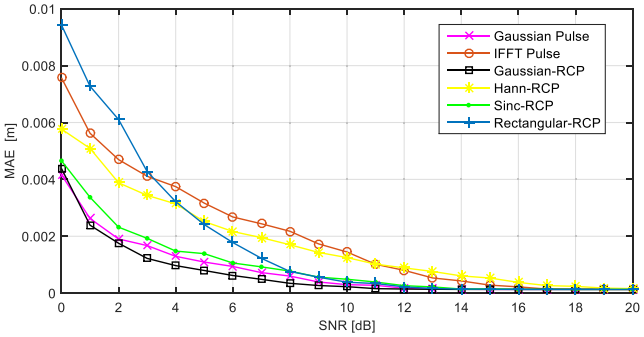

FIGURE 15. MAE with a correlation receiver.

B. ENERGY DETECTOR PERFORMANCE WITH A FIXED THRESHOLD

Figure 16 presents the MAE of the range estimation using an energy detector with a fixed threshold $\xi = 1$ for SNR values from 5 dB to 30 dB. This shows that the Gaussian pulse, Gaussian-RCP, and Sinc-RCP have the best performance which is similar, while the Hann-RCP, IFFT pulse, and Rectangular-RCP have the worst performance. For example, when SNR=14 dB, the MAE of the Gaussian Pulse, Gaussian-RCP and Sinc-RCP is about 0.22 m, while that of the Rectangular-RCP is about 0.62 m. When SNR>19 dB, the MAE of the Rectangular-RCP decreases to 0.05 m, while the error with the other waveforms is less than 0.02 m. Figure 17 presents the MAE of the range estimation using an energy detector with a fixed threshold $\xi = 0.6$ for SNR values from 5 dB to 30 dB. In general, the MAE is smaller than that in Fig. 16, so the threshold is a key parameter in determining the performance of energy detector methods.

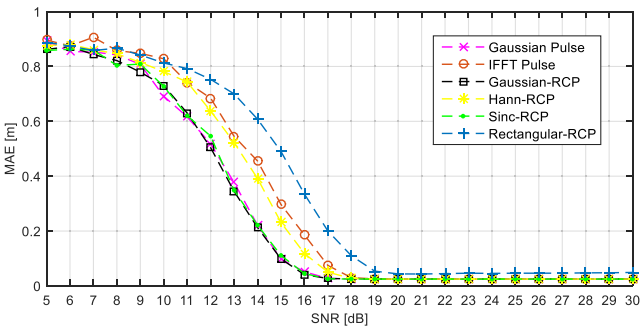

FIGURE 16. MAE with a fixed threshold $\xi = 1$.

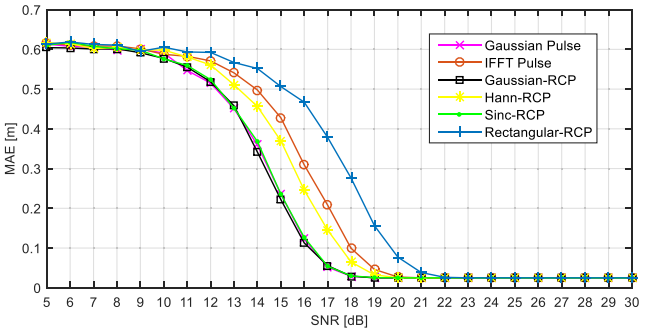

FIGURE 17. MAE with a fixed threshold $\xi = 0.6$.

C. ENERGY DETECTOR PERFORMANCE WITH A DYNAMIC THRESHOLD

Figure 18 presents the MAE of the range estimation based on the fitted curves given in Section 4.3 for SNR values from 5 dB to 30 dB. This shows that a dynamic threshold provides better performance than a fixed threshold. For example, when SNR=5 dB, the MAE with the dynamic threshold is about 0.5 m, but with a fixed threshold $\xi = 0.6$ is about 0.6 m and with $\xi = 1$ is close to 0.9 m. For all waveforms, the dynamic threshold accuracy at low SNRs is better than with a fixed threshold. From a waveform perspective, the same conclusions can be drawn as with a fixed threshold, namely, the Gaussian pulse, Gaussian-RCP and Sinc-RCP waveforms

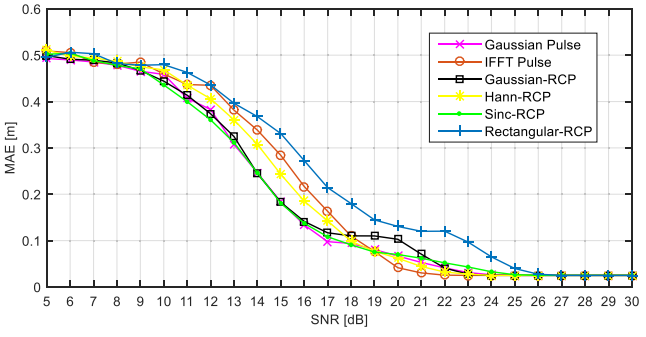

FIGURE 18. MAE with a dynamic threshold.

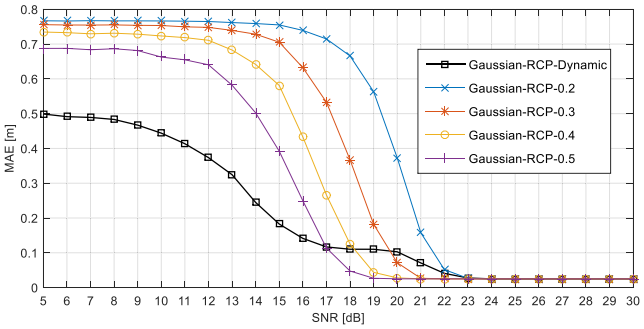

FIGURE 19. MAE with different thresholds.

are the best, while the Rectangular-RCP waveform provides the worst performance.

Figure 19 presents the MAE with different thresholds for the Gaussian-RCP. This shows that the dynamic threshold provides better performance than with the fixed thresholds for most SNR values, particularly when the SNR is less than 17 dB. When the SNR is greater than 23 dB, all thresholds provide similar performance of about 2 cm. Considering the results in Figures 16 to 19, it can be concluded that a dynamic threshold is a better choice for an energy detector.

D. mmWAVE WAVEFORM SELECTION

For both the correlation receiver and energy detector, the accuracy of the Gaussian-RCP, Gaussian pulse, and Sinc-RCP waveforms is the best, and the Rectangular-RCP waveform provides the worst performance. In a vehicular environment, a Doppler shift typically exists, in which case the PSD should be as close to ideal as possible. Thus, the energy in the signal sidelobes should be low to have good ranging accuracy. Figures 2 and 6 show that there are no sidelobes in the Gaussian-RCP and Gaussian pulse with a PSD greater than -150 dB/GHz, so they should provide the best ranging accuracy. Conversely, Figures 4, 7, 8 and 9 indicate that the sidelobes have a PSD of -14 dB/GHz in the Rectangular-RCP, -22 dB/GHz in the IFFT pulse, -25 dB/GHz in the Sinc-RCP, and -28 dB/GHz in the Hann-RCP, so the accuracy of the Rectangular-RCP is the worst. The Sinc-RCP is better than the Hann-RCP and IFFT pulse because it has a PSD which is more concentrated in the mainlobes.

E. COMPUTATIONAL COMPLEXITY

Equation (23) indicates that the computational complexity of a correlation receiver is primarily due to the correlation operation. An energy detector consists of a square-law device followed by an integrator. Employing a dynamic threshold is more complex than a fixed threshold, but the difference should not be substantial. In order to compare the computational complexity of these methods, 1000 iterations were generated for the correlation receiver, energy detector with a fixed threshold and energy detector with a dynamic threshold. The average execution time is given in Table 3.

This shows that the energy detector execution times with the fixed and dynamic thresholds are similar, but the time for the correlation receiver is substantially higher. Thus, an energy detector is a more practical solution for real-time applications.

TABLE 3. Average execution time with three methods.

Method	Execution Time
correlation receiver	1219 ms
energy detector with a dynamic threshold	0.683 ms
energy detector with a fixed threshold	0.610 ms

VI. CONCLUSION

In order to meet the demands of vehicular environments, six millimeter wave (mmWave) waveforms were considered for timing estimation. These waveforms were evaluated using both an energy detector and a correlation receiver. Performance results were presented which show that with all estimation methods, the Gaussian-RCP, Gaussian pulse, and Sinc-RCP waveforms provide the best performance, while the Rectangular-RCP waveform has the worst performance. While the accuracy of the correlation receiver is better than that of the energy detector, it is more complex due to the fact that a high sampling frequency and channel estimation are required. Further, it was shown that the energy detector performance with a dynamic threshold is much better than that with a fixed threshold. Thus, an energy detector is an excellent choice for vehicle positioning using D2D communications in emerging 5G cellular networks. To date, there are no generally accepted 5G waveforms, so six impulse radio (IR) waveforms were investigated which are well suited to accurate ranging. Once 5G standards have been developed with candidate waveforms, they can be compared with the waveforms considered in this paper.

REFERENCES

[1] (Jun. 30, 2016). *World Health Organization. Global Status Report on Road Safety 2013: Supporting a Decade of Action*. [Online]. Available: http://www.who.int/iris/bitstream/10665/78256/1/9789241564564_eng.pdf
[2] X. Guan, Y. Huang, Z. Cai, and T. Ohtsuki, "Intersection-based forwarding protocol for vehicular ad hoc networks," *Telecommun. Syst.*, vol. 62, no. 1, pp. 67–76, 2016.
[3] G. J. Han, Y. H. Dong, H. Guo, L. Shu, and D. P. Wu, "Cross-layer optimized routing in wireless sensor networks with duty cycle and energy harvesting," *Wireless Commun. Mobile Comput.*, vol. 15, no. 16, pp. 1957–1981, Nov. 2015.
[4] B. H. Lee, J. H. Song, J. H. Im, S. H. Im, M. B. Heo, and G. I. Jee, "GPS/DR error estimation for autonomous vehicle localization," *Sensors*, vol. 15, no. 8, pp. 20779–20798, Aug. 2015.
[5] F. V. Diggelen, "Precise positioning using GLONASS," *Geomatics Info Mag.*, vol. 12, no. 12, pp. 61–63, 1998.
[6] G.-L. Sun and Z.-M. Ding, "Working method improvements of Beidou satellite system," *Acta Electronica Sinica*, vol. 29, no. 9, pp. 1217–1220, 2001.
[7] W. Wei and Y. Qi, "Information potential fields navigation in wireless ad-hoc sensor networks," *Sensors*, vol. 11, no. 5, pp. 4794–4807, May 2011.
[8] M. Simic and P. Pejovic, "Positioning in cellular networks," in

Cellular Networks—Positioning, Performance Analysis, Reliability. Rijeka, Croatia: InTech, 2011, pp. 51–76.

[9] V. Singh, I. Gupta, and H. O. Gupta, "ANN-based estimator for distillation using Levenberg-Marquardt approach," *Eng. Appl. Artif. Intell.*, vol. 20, no. 2, pp. 249–259, Mar. 2007.

[10] G. Han, A. Qian, J. Jiang, N. Sun, and L. Liu, "A grid-based joint routing and charging algorithm for industrial wireless rechargeable sensor networks," *Comput. Netw.*, vol. 101, pp. 19–28, Jun. 2016.

[11] C. Vu, Z. Cai, and Y. Li, "Distributed energy-efficient algorithms for coverage problem in adjustable sensing ranges wireless sensor networks," *Discrete Math. Algorithms Appl.*, vol. 1, no. 3, pp. 299–317, 2009.

[12] Z. Xiao, J. Bai, G. Y. Ma, J. T. Fan, and K. C. Yi, "Research on positioning enhancement scheme of CAPS via UWB pseudolite," *Sci. China-Phys. Mech. Astron.*, vol. 55, no. 4, pp. 733–737, Apr. 2012.

[13] C. W. Tsai, H. H. Cho, T. K. Shih, J. S. Pan, and J. J. P. C. Rodrigues, "Metaheuristics for the deployment of 5G," *IEEE Wireless Commun.*, vol. 22, no. 6, pp. 40–46, Dec. 2015.

[14] T. S. Rappaport *et al.*, "Millimeter wave mobile communications for 5G cellular: It will work!" *IEEE Access*, vol. 1, pp. 335–349, May 2013.

[15] J. Gozalvez, "Samsung electronics sets 5G speed record at 7.5 Gb/s [mobile radio]," *IEEE Veh. Technol. Mag.*, vol. 10, no. 1, pp. 12–16, Mar. 2015.

[16] M. R. Akdeniz *et al.*, "Millimeter wave channel modeling and cellular capacity evaluation," *IEEE J. Sel. Areas Commun.*, vol. 32, no. 6, pp. 1164–1179, Jun. 2014.

[17] A. M. Petroff, "Ultra wideband two-way time-of-flight distance measurement provides sub-centimeter range measurement accuracy," in *Proc. Radio Sci. Meeting, AP-S Symp. USNC-URSI*, Jul. 2015, p. 212.

[18] *Next Generation Wireless Communication (5G): Transforming the Wireless User Experience*, accessed on Jul. 30, 2016. [Online]. Available: http://blogs.intel.com/intellabs/2013/07/15/next-generation-wireless-communication-5g-transforming-the-wireless-user-experience

[19] F. Schaich, T. Wild, and Y. Chen, "Waveform contenders for 5G—Suitability for short packet and low latency transmissions," in *Proc. IEEE 79th Veh. Technol. Conf. (VTC Spring)*, pp. 1–5, May 2014.

[20] *IEEE Standard for Information Technology—Telecommunications and Information Exchange Between Systems—Local and Metropolitan Area Networks—Specific Requirement Part 15.4: Wireless Medium Access Control (MAC) and Physical Layer (PHY) Speci Cations for Low-Rate Wireless Personal Area Networks (WPANs)*, accessed on Jul. 30, 2016. [Online]. Available: http://standards.ieee.org/getieee802/download/802.15.4a-2007.pdf

[21] G. Han, L. Liu, J. Jiang, L. Shu, and G. Hancke, "Analysis of energy-efficient connected target coverage algorithms for industrial wireless sensor networks," *IEEE Trans. Ind. Informat.*, vol. PP, no. 99, pp. 1–14, Apr. 2016.

[22] Q. Chen, S. Y. Cheng, H. Gao, J. Z. Li, and Z. P. Cai, "Energy-efficient algorithm for multicasting in duty-cycled sensor networks," *Sensors*, vol. 15, no. 12, pp. 31224–31243, Dec. 2015.

[23] X.-R. Cui, H. Zhang, and T. A. Gulliver, "Threshold selection for ultra-wideband toa estimation based on neural networks," *J. Netw.*, vol. 7, no. 9, pp. 1311–1318, 2012.

[24] L. Y. Song, H. L. Zou, and T. T. Zhang, "A low complexity asynchronous UWB TDOA localization method," *Int. J. Distrib. Sens. Netw.*, vol. 11, p. 9, Jan. 2015.

[25] Y. L. Sun, Y. B. Xu, C. Li, and L. Ma, "Kalman/map filtering-aided fast normalized cross correlation-based Wi-Fi fingerprinting location sensing," *Sensors*, vol. 13, no. 11, pp. 15513–15531, Nov. 2013.

[26] S. Tomic, M. Beko, and R. Dinis, "Distributed RSS-based localization in wireless sensor networks based on second-order cone programming," *Sensors*, vol. 14, no. 10, pp. 18410–18432, Oct. 2014.

[27] J. Xu, M. D. Ma, and C. L. Law, "Cooperative angle-of-arrival position localization," *Measurement*, vol. 59, pp. 302–313, Jan. 2015.

[28] Z. Sahinoglu, S. Gezici, and I. Güvenc, *Ultra-Wideband Positioning Systems: Theoretical Limits, Ranging Algorithms, and Protocols*. Cambridge, U.K.: Cambridge Univ. Press, 2008.

[29] T. Adnan, S. Datta, and S. MacLean, "Efficient and accurate sensor network localization," *Pers. Ubiquitous Comput.*, vol. 18, no. 4, pp. 821–833, 2014.

[30] Y.-H. Huang, K.-H. Fan, and W.-S. Hsieh, "Message authentication scheme for vehicular ad-hoc wireless networks without RSU," *J. Inf. Hiding Multimedia Signal Process.*, vol. 6, no. 1, pp. 113–122, Jan. 2015.

[31] L. Wang, T. K. Hon, J. D. Reiss, and A. Cavallaro, "Self-localization of ad-hoc arrays using time difference of arrivals," *IEEE Trans. Signal Process.*, vol. 64, no. 4, pp. 1018–1033, Feb. 2016.

[32] J. Guo, H. Zhang, Y. Sun, and R. Bie, "Square-root unscented Kalman filtering-based localization and tracking in the Internet of things," *Pers. Ubiquitous Comput.*, vol. 18, no. 4, pp. 987–996, 2014.

[33] X. Cui, J. Li, C. Wu, and J.-H. Liu, "A timing estimation method based-on skewness analysis in vehicular wireless networks," *Sensors*, vol. 15, no. 11, p. 28942–28959, 2015.

[34] H. Zhang, X.-R. Cui, and T. A. Gulliver, "Threshold selection for ultra-wideband TOA estimation based on skewness analysis," in *Ubiquitous Intelligence and Computing* (Lecture Notes in Computer Science). Heidelberg, Germany: Springer Verlag, 2011, pp. 503–513.

XUERONG CUI (M'16) received the master's degree in computer application technology from the China University of Petroleum in 2003, and the Ph.D. degree in information science and engineering from the Ocean University of China in 2012. He joined the Department of Computer and Communication Engineering, China University of Petroleum, in 2003. From 2015 to 2016, he was with the University of Victoria as a Visiting Scholar. His research interests include positioning based on wireless communication, intelligent transport system, Internet of Vehicles, global navigation satellite system, millimeter-wave wireless communication, and ultrawideband radio systems.

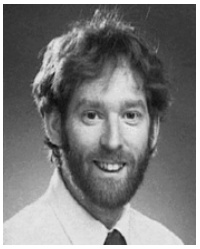

THOMAS AARON GULLIVER (S'81–M'90–SM'96) received the B.Sc. (Eng.) and M.Sc. (Eng.) degrees from the University of New Brunswick, Fredericton, New Brunswick, in 1982 and 1984, respectively, and the Ph.D. degree from the University of Victoria in 1989, all in electrical engineering. In 2002, he was a fellow of The Engineering Institute of Canada. In 2012, he was a fellow of The Canadian Academy of Engineering. He is currently a Professor with the Department of Electrical and Computer Engineering, University of Victoria. His research interests include ultrawideband and spread spectrum communication systems, mobile and personal communications, OFDM, smart grid and green communications, algebraic coding theory, turbo codes and iterative decoding, and error control coding for computer memories.

JUAN LI received the B.S. degree in control theory and engineering and the master's degree in applied electronic technology from the China University of Petroleum in 2001 and 2004, respectively, and the Ph.D. degree in computer system architecture from the Ocean University of China in 2016. Since 2004, she has been a Lecturer with the Department of Computer and Communication Engineering, China University of Petroleum. Her research interests include positioning based on wireless communication and intelligent transport system.

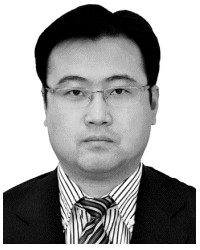

HAO ZHANG was born in 1975. He received the bachelor's degree in telecom engineering and industrial management from Shanghai Jiao Tong University, China, in 1994, the M.B.A. degree from the New York Institute of Technology, USA, in 2001, and the Ph.D. degree in electrical and computer engineering from the University of Victoria, Canada, in 2004. From 1994 to 1997, he was the Assistant President of ICO Global Communication, China. He is currently a Professor with the Department of Electronic Engineering, Ocean University of China, and an Adjunct Assistant Professor with the Department of Electrical and Computer Engineering, University of Victoria. His research interests include ultrawideband radio systems, MIMO wireless systems, and spectrum communications.